RESEARCH

Subnanosecond 1.3-µm laser for generating picosecond pulses in the long-wavelength infrared range

Ya-Po Yang[1,2] · Jheng-Yu Lee[1,2] · Feng-Yen Su[2] · Hsu-hsin Chu[2] · Jyhpyng Wang[2,3]

© The Author(s), under exclusive licence to Springer-Verlag GmbH Germany, part of Springer Nature 2024

Abstract

We report the development of a seeded diode-pumped 1338-nm Nd:YAG amplifier which delivers 400-ps, 6-mJ, single-frequency pulses every half second with a fluctuation of ∼ 0.7%. A highly stable pulsed current controller is constructed to drive an 808-nm diode laser array that ensures the high stability of the laser. Numerical calculations show that 9.2 µm or 10.2-µm picosecond (<10 ps) pulses with 100-µJ energy can be generated by mixing the 1338-nm 6-mJ pulses with 1540-nm chirped pulses in a BGGSe nonlinear crystal and compressing the pulse with a grating compressor.

1 Introduction

High-power Nd:YAG lasers operating at 1.3 µm have supported many distinctive applications even though they are less popular than the same medium operating at 1.06 µm. They have been used in the resection of pulmonary metastases and dental surgery due to their tenfold higher absorption in water and good blood hemostasis compared with the common 1064-nm lasers [1–3]. Doubling and tripling the frequency produces bright red and blue lasers for laser display [4]. Eighth-harmonic generation of 1.3-µm lasers has been demonstrated for photoemission spectroscopy and Raman spectroscopy [5]. HBr molecular laser with highly efficient cascade lasing has been realized by optically overtone-pumping with 1.34 µm Nd:YAG laser [6]. Mixing a 1.3-µm pulse with a 1.4–1.6-µm pulse generates an idler pulse in the long-wavelength infrared (LWIR) range of 8–15 µm which is useful for many applications, ranging from molecular spectroscopy and atmospheric remote sensing [7] to seeding terawatt-class CO_2 amplifiers [8, 9].

Applications utilizing nonlinear frequency conversion benefit from pulsed lasers with high peak power. Using a 1.3-µm pulsed laser as the pump laser is advantageous in avoiding two-photon absorption in nonlinear crystals. This is because nonlinear crystals with wide transparency ranges such as GaSe (0.62–19 µm) [10], $BaGa_2GeSe_6$ (0.6–18 µm) [11], etc. have two-photon absorption edges around 1 µm which limits the pump intensity of popular 1053-nm and 1064-nm lasers. Many approaches for generating 1.3-µm pulses have been published in the literature, including Q-switching and mode-locking [12–16]. Kilojoule-class iodine photodissociation lasers and chemical oxygen-iodine lasers delivering 1.3-µm pulses have been constructed [17, 18]. Limited by the laser-induced damage threshold of nonlinear crystals, the trade-off between the aperture size of a nonlinear crystal and the peak intensity of its pump laser sets the pulse duration in the 50–500 ps range for millijoule-level pumping. Mode-locked lasers with narrow bandwidth (< 0.1 nm) can produce pulses with duration in such a range; however, the pulse duration cannot be tuned easily. Gain-switching and Q-switching can produce nanosecond to picosecond pulses [19], but the timing jitter is typically comparable to their pulse duration. This is undesirable for applications such as wave mixing where tight synchronization of two lasers is required. In addition, pump lasers with single-longitudinal mode are critical for nonlinear frequency conversion since multi-longitudinal mode beating causes amplitude modulation, or spectral modulation for chirped pulses, of signal and idler pulses. Chip-scale electro-optic intensity modulator based on Mach-Zehnder interferometer

✉ Ya-Po Yang
   albert7015@gmail.com

1   Molecular Science and Technology, Taiwan International Graduate Program, Academia Sinica, National Central University, Taipei, Taiwan

2   Department of Physics, National Central University, Taoyuan 320317, Taiwan

3   Institute of Atomic and Molecular Sciences, Academia Sinica, Taipei 106319, Taiwan

has reached a modulation frequency beyond 100 GHz and thus can be used to generate optical pulses with durations down to a few picosecond [20]. With a wavelength-tunable, single-frequency, continuous-wave (CW) laser, an optical pulse with controlled shape and central wavelength can be generated with an intensity modulator driven by an electrical pulse generator; Yet, typical pulse energy is below 20 pJ due to its limited input CW power of <100 mW and an insertion loss of >5 dB. For these reasons, a 1.3-μm laser amplifier is needed to boost the pulse energy for practical applications.

Iodine photodissociation amplifiers have been demonstrated for amplifying 1315-nm pulses down to ~250 ps [21]; however, this type of gaseous amplifier is bulky and inefficient. Neodymium-doped crystals are more attractive alternatives for amplifying 1.3-μm pulses, because they can be efficiently pumped by diode lasers. In comparison with other popular neodymium-doped crystals such as Nd:glass, Nd:YVO$_4$, and Nd:YLF, Nd:YAG crystal possesses better mechanical and thermal properties. Nd:YAG also has a long fluorescence lifetime of ~230 μs [22]. These properties make Nd:YAG a preferable gain medium for constructing diode-pumped high-power lasers. Particularly interesting to LWIR generation, the $^4F_{3/2} \rightarrow {}^4I_{13/2}$ transision of Nd:YAG crystal has two main 1.3-μm lines with comparable stimulated emission cross sections of 8.7×10^{-20}cm^2 at 1319 nm and 9.2×10^{-20}cm^2 at 1338 nm [22]. Nonlinear mixing of 1319-nm/1338-nm pulses with 1540-nm pulses from an Er:fiber laser generates 9.2-μm/10.2-μm pulse, whose spectrum coincides with the 9R-/10R-branch emission spectrum of the CO_2 molecule and can be amplified by a CO_2 amplifier.

Laser energy stability is one of the key requirements to produce consistent results in wave-mixing experiments or laser-plasma interactions [23–25] due to their nonlinear nature. According to the theory described in Ref. [26], the output energy fluctuation of a regenerative amplifier depends inversely on the ratio of small-signal gain to loss coefficient. Considering a Nd:YAG regenerative amplifier with typical 15% round-trip loss and round-trip gain of 1.7 at 1338 nm, a 1% fluctuation of pump energy results in ~4% fluctuation in maximum output energy. Therefore, a stable current controller is critical to the stability of a diode laser and consequently the output energy stability of a diode-pumped regenerative amplifier.

In this paper, we report the development of a diode-pumped 1338-nm laser delivering 400-ps single-frequency pulses with an energy up to 6 mJ and a shot-to-shot energy fluctuation of ~0.7%. The laser consists of the following parts:

(1)   A 400-ps seed generator based on a 3-mW external-cavity diode laser and an intensity modulator driven by a subnanosecond pulse generator (Sec. 2).

(2)   A linear-mode pulsed current controller with high stability of ~0.0025%-rms and low drift of ~12.5 ppm/hr (Sect. 3).

(3)   A diode-pumped Nd:YAG regenerative amplifier with a total gain over 10^{10} (Sect. 4).

Such a sub-ns 1338-nm laser can be utilized to generate sub-millijoule picosecond 10.2-μm pulses by difference frequency generation (DFG) with sub-ns 1.5-μm chirped pulses (Sect. 5) for seeding terawatt-class CO_2 amplifiers [8].

2 Generation of a 400-ps 1.3-μm seed

The sub-ns 1.3-μm seed consists of a CW laser, an electro-optic intensity modulator, and a sub-ns electrical pulse generator. The wavelength of the CW laser must be precisely tuned and maintained for a long period since the gain bandwidth of Nd:YAG is only ~1 nm at 1.3-μm, so we chose to construct an external-cavity diode laser (ECDL) in Littrow configuration as shown in Fig. 1. The ECDL is based on an InP gain chip (SAF1144H, Thorlabs) with 10% reflectance at one end and < 0.01% reflectance at the other end. A 1200-groove/mm ruled grating and the 10%-reflectance facet of the gain chip form a laser cavity. The first-order diffraction of the grating feeds back to the gain chip, providing a wavelength tuning range from 1310 nm to 1345 nm. The grating is preset with a thermoplastic adhesive and a 3-axis mirror mount. Once the lasing wavelength and optimal alignment are reached by manual tuning, a two-part epoxy is applied on the two faces of a stainless steel block to bond the grating and a thermoelectric cooler. After the epoxy is cured, the mirror mount can be disassembled by heating the thermoplastic adhesive, and a wavelength-tuned ECDL without any movable part is obtained. The output power is >3 mW at 1338 nm after coupling into a polarization-maintaining single-mode optical fiber with a prism pair and an aspheric lens. The cavity length is ~15 mm corresponding to a free-spectral range of ~10 GHz. The laser power, measured with a 12-GHz photodiode and a 15-GHz sampling scope (Pico Technology, UK), is stable without beating fluctuation,
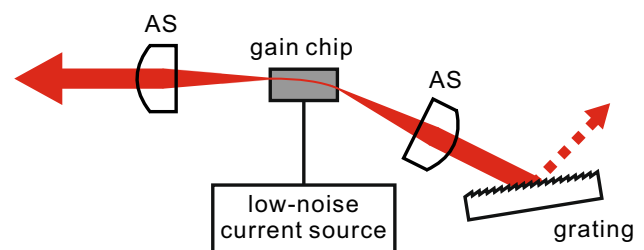

Fig. 1 Schematic of the single-frequency 1.3-μm ECDL laser built on a thermoelectric cooler. AS: aspheric lens

indicating that the laser operates at single-longitudinal mode without mode hopping.

The 1338-nm CW laser is amplitude-modulated with a 10-GHz fiber-coupled Mach-Zehnder intensity modulator (Optilab, USA) driven by a sub-ns electrical pulse generator to produce sub-ns optical pulses. The idea of generating sub-ns electrical pulses is that emitter-coupled logic (ECL) gates are utilized to produce fast edges with a transition time of ∼300 ps. A sub-ns duration is achieved by a positive-edge detector circuit as shown in Fig. 2. An AND logic gate operates on an input pulse and its delayed inversion. The pulse duration can be varied by changing the length of the delay line. After amplifying the generated sub-ns electrical pulse by a 2.5-GHz RF amplifier (Mini-Circuits, USA), the pulse amplitude can be as high as 4 volts. A sub-ns optical pulse with ∼0.2-pJ energy is generated by the intensity modulator. The pulse duration of ∼400 ps and the timing jitter of ∼10 ps-rms with respect to its trigger are measured with a 12-GHz photodiode and a 15-GHz sampling scope.

Driving the intensity modulator from destructive interference to constructive interference requires a half-wave voltage V_π of ∼5 V; however, it is better to drive the modulator below 3 V to avoid significant waveform distortion since the output optical power is proportional to $\sin^2(\pi V_d/(2V_\pi))$, where V_d is the driving voltage. In the small-signal regime, the optical power can be approximated to the squre of the driving electrical pulse. As a result, if the electrical pulse is modeled by a Gaussian pulse, the duration of the optical pulse will be $1/\sqrt{2}$ of the duration of the electrical pulse. Care should be taken when using lithium niobate Mach-Zehnder modulators. The on-off extinction ratio of the modulator should be larger than 30 dB because the output CW background will be amplified together with the sub-ns optical pulse in a boost amplifier. This will lead to a large energy fluctuation of the sub-ns pulse due to gain competition. Moreover, the CW background could be drifting as the
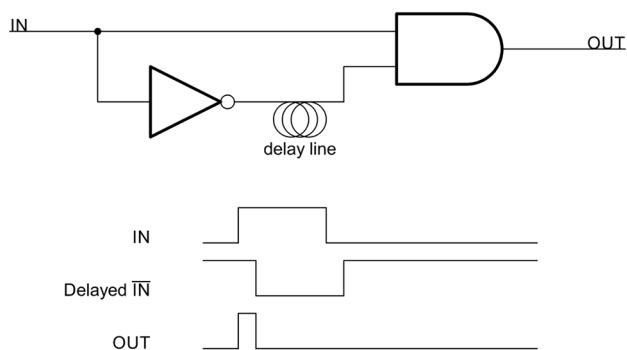
interference conditions vary with temperature, bias electric field distribution, etc. [27]. To overcome this problem, a digital lock-in detection circuit [28] and a photodiode are adopted to obtain an error signal from the first-order derivative of the output power. A digital proportional-integral controller calculates the error signal and feeds back to the bias port of the modulator. Thereby, a minimum CW background and hence the optimal temporal contrast can be maintained.

# 3 Highly stable pulsed current controller

3.1 Circuit description—linear current regulator

A detailed comparison of different types of pulsed current controllers, including techniques of pulse-forming network, switch-mode regulation, linear-mode regulation, etc., can be found in Ref. [29]. The switched-mode and linear-mode circuits implement an active feedback system which meets the basic requirement for a stable current controller. The switched-mode current regulation scheme is commonly used in commercial products to realize high electrical efficiency and wide voltage compliance. However, it has significant drawbacks including large amplitude fluctuation due to hysteretic control, bulky inductors withstanding currents of hundreds of amperes, and large electromagnetic interference [29]. To achieve high stability and low electromagnetic interference, the linear current regulation scheme is preferable regardless of its moderate electrical efficiency when a low voltage load is used. Design concepts for constructing a direct-current (DC) linear current controller with high performance can be found in Ref. [30]. To extend the capability of the controller to our targeted applications such as driving diode laser array (DLA) for pumping solid-state lasers, we introduced a floating control design in combination with a tailored reference pulse generator.

Figure 3 shows the main schematic of the pulsed current controller based on linear-mode circuit. The three 6600-µF aluminum electrolytic capacitors are charged by the −24-V supply. The 2-mΩ sense resistor is placed in series with the load to create a voltage drop with respect to the common potential (COM), which is not equal to the ground potential (GND). To handle up to 250-A current in a duration of 300 µs and control the current passing through the DLA, two N-channel MOSFETs are placed between the load and the sense resistor. The MBR2H200 diode reversely shunts the DLA to prevent reverse voltage on the DLA. The reference pulse generator is used to produce a stable pulse as a reference voltage waveform between the non-inverting input of the LT1028 op-amp and COM. It is described in detail in the next subsection.

Current regulation is performed by comparing the voltage between non-inverting and inverting inputs of the LT1028,

Fig. 2 Schematic and timing diagrams of the sub-ns electrical pulse generator. The circuit is composed of an ECL AND gate, an ECL inverter, and a delay line

Fig. 3 Schematic of the pulsed current controller. The circuit can sink up to 250-A, 300-μs pulse current
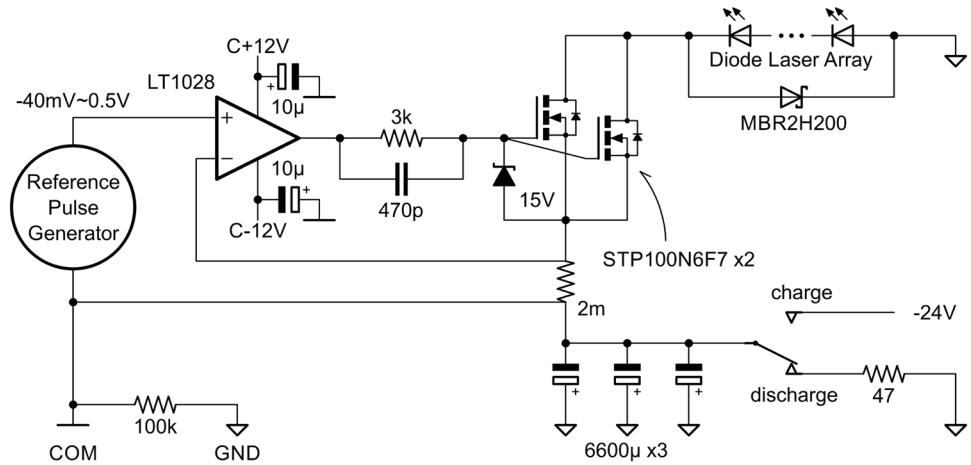
and then the LT1028 controls the gates of the MOSFETs through an RC lead-compensator which provides a large enough phase margin and reduces the tendency to oscillate. In practice, the selected values of these passive components depend on circuit layout and characteristics of parts. The current flowing through the MOSFETs is adjusted by the feedback loop until the voltage difference of the sense resistor is equal to the voltage at the non-inverting input of the LT1028. As a result, the output current waveform follows the voltage of the reference pulse precisely.

Components are selected to achieve consistent performance and minimize temperature-induced drift. The 2-mΩ Bourns sense resistor (CSS4J-4026K) features a four-terminal configuration. Utilizing a four-terminal sense resistor is crucial as the temperature coefficients of copper and SnPb solder are roughly 100 times larger than that of the sense resistor [31, 32]. Therefore, a short copper strip or a small amount of solder on a printed circuit board (PCB) can ruin the accuracy and stability of a standard two-terminal sense resistor.

In order to prevent the output voltage of op-amps from reaching their power supply rail, some power supplies are

floated on COM. The character "C" in Figs. 3 and 4 represents the voltage potential of COM. With this floating control design, the controller allows a wide supply voltage range since the current control circuit floats with the supply voltage. Furthermore, voltage bounces of common potential will occur when a large current flows through a tiny resistance on a PCB strip or power supply capacitors, resulting in distortion of output current pulse as well as incorrect pulse amplitude. As the voltage bounces vary shot by shot, the stability performance will be reduced. The floating control design is immune to voltage bounces, since the reference pulse generator and the sense terminal of the sense resistor share the same common potential.

3.2 Circuit description—reference pulse generator

Figure 4 shows the schematic of the reference pulse generator. The reference pulse output is biased at a negative offset, and its waveform is composed of a top-hat pulse and a plateau pulse. The negative offset plays an important role in eliminating any positive offset voltage at the non-inverting input of the LT1028. Since the current controller has

Fig. 4 Schematic of the reference pulse generator. Zener diodes (ZD) are LM4040C25 having a reverse-biased voltage of 2.5 V
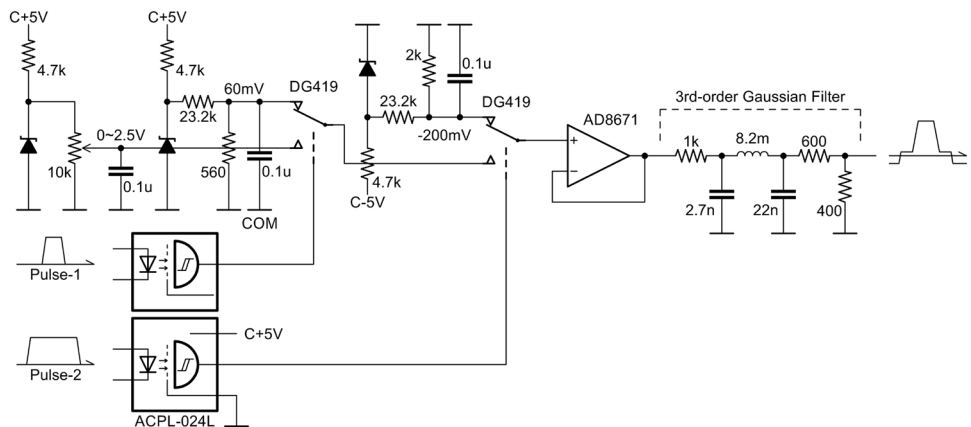
a transconductance of 500 A/V, a mere 1-mV offset voltage will draw 0.5 A from the −24-V power supply. When the circuit is idling, the output of the LT1028 stays near its negative rail voltage, so negligible current flowing through the MOSFETs is guaranteed. An undesirable effect of such a design is that the LT1028 will produce an overshoot pulse when a positive transition arrives at its non-inverting input, and a large current spike will be found at the load accordingly. This is because the LT1028 typically takes a few μs to recover from saturation. To avoid this effect, a plateau pulse, wider than the top-hat pulse, is intentionally added to the top-hat pulse so that the LT1028 recovers to a normal operating condition with a mild spike, as shown in Fig. 5.
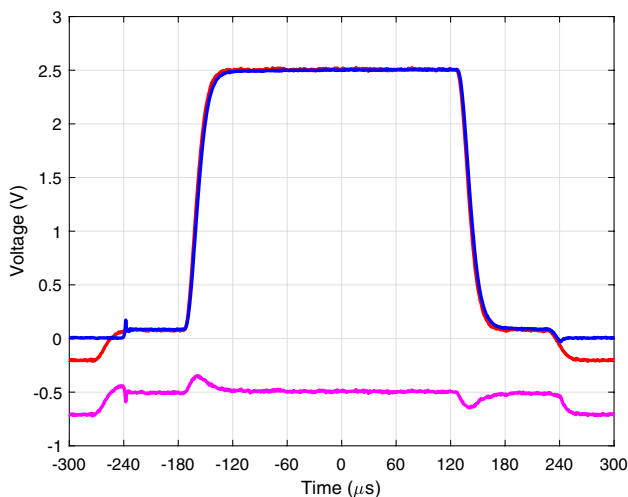

Fig. 5 Measured waveforms of the reference pulse with ×5 magnification (red line) and output current at 250 A (blue line)

The current spike is tuned by the amplitude of the plateau pulse to keep it below the lasing threshold of the DLA such that the DLA would not emit an undesired pulse.

In order to generate the required waveform, the two DG419 analog switches are controlled by two pulses through the ACPL-024 L dual digital optocoupler. When the circuit is idling, the voltage at the non-inverting input of the AD8671 op-amp stays at −200 mV with respect to COM. Pulse-2 switches the voltage to 60 mV creating the plateau. Pulse-1 switches the voltage to create the top-hat pulse with an amplitude from 0 V to 2.5 V. Subsequently, the AD8671 op-amp buffers the generated signal to a passive third-order Gaussian filter [33], whose −3-dB frequency is ~16 kHz, to smoothen transition edges.

3.3 Results

Measured waveforms of the reference pulse and the output current are shown in Fig. 5. A low waveform distortion of ~0.4% is measured within the range of ±180 μs under full-current condition. The distortion D is defined by

$$D = \frac{1}{n}\sqrt{\sum_{i=1}^{n}\left(\frac{\Delta V_i}{V_i}\right)^2}, \tag{1}$$

where ΔV_i and V_i are the i-th sample of the voltage difference between the two signals and the reference pulse, respectively; n is the number of samples under calculation.

Figure 6 shows measured time-integrated current pulses of the current controller using twelve FR307 diodes (6 in series, 2 in parallel) as the load to simulate a DLA and

Fig. 6 Time-integrated current pulse measurement of the current controller. **a** Startup and long-term performance. The red trend line indicates a slope of 12.5 ppm/hr. The histogram on the right shows accumulated data from the 3600th shot to the 18000th shot (4 h), indicating a Gaussian-like distribution. **b** Moving standard deviation σ of 120 shots shows a short-term shot-to-shot fluctuation of ~ 25 ppm-rms
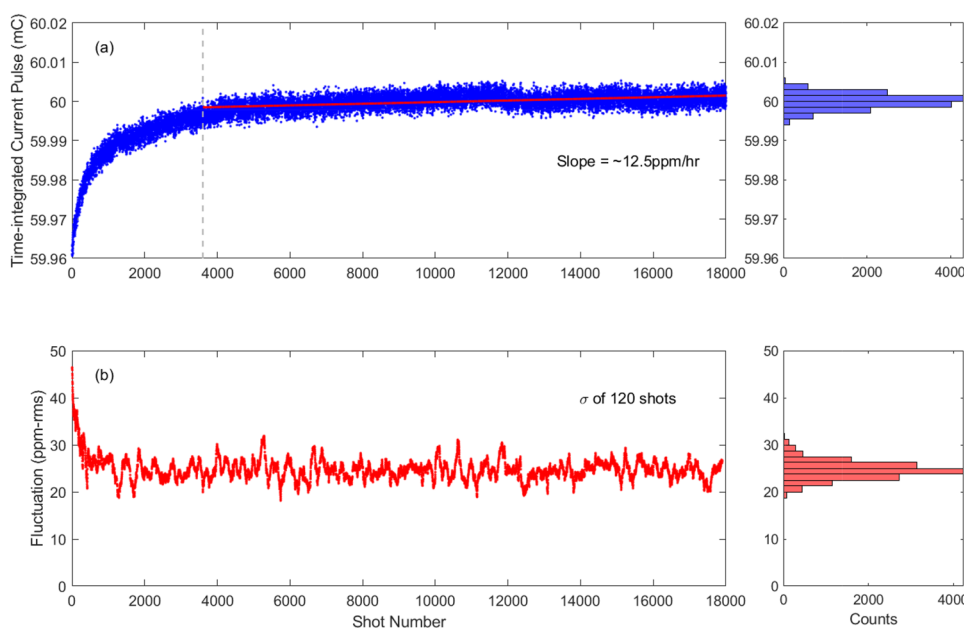
operating at 250-A current with a duration of 300 μs. To measure a ppm-level fluctuation, we added a stable −2.1-V offset voltage to the current monitor signal and used a Tektronix MSO44 oscilloscope with a vertical span of 50 mV to fully utilize the 12-bit resolution. Time integration of current pulses is done by calculating the area of each pulse over the flat region of ±120 μs.

Before measurement, all the instruments are warmed up for more than 3 h except the current controller under test. We ran the current controller 1 shot per second for 5 h due to limited built-in storage capacity of the oscilloscope. A shot-to-shot fluctuation of ~25 ppm-rms or ~0.0025% rms in 120-shot, 120-s samples, and a long-term drift of ~12.5 ppm/hr under a typical laboratory environment are achieved 1 h after startup. The output energy fluctucation of the DLA is similar to the current controller. The measured temperature coefficient of the controller is ~100 ppm/°C at an ambient temperature around 23 °C.

4 Diode-pumped Nd:YAG regenerative amplifier

Nd:YAG crystal is selected as the gain medium for amplifying the sub-ns 1338-nm seed. The Nd:YAG gain medium is pumped with an 808-nm DLA driven by the pulsed current controller described in Sect. 3. The DLA is focused with an $f = 25.4$ mm plano-convex cylindrical lens and an $f = 38.1$ mm bi-convex lens. With a quasi-CW pump intensity of ~3.7 kW/cm^2, at a pump power of ~730 W and a pump duration of 300 μs, a population inversion density N_0 of ~2.5×10^{18}/cm^3 can be achieved in a 5-mm-thick 1.1-at% Nd:YAG disk. The Nd:YAG disk is antireflection coated at one surface and high-reflection coated at the other surface for both pumping and lasing wavelength. A gain of ~1.7 at 1338 nm for one bounce of the pumped Nd:YAG disk is measured. To boost the pulse energy from 0.2 pJ to the required millijoule level, a regenerative amplifier is needed. Figure 7 shows a schematic diagram of the linear regenerative amplifier. The cavity of the amplifier is constructed with

several flat mirrors, a convex mirror with a radius of curvature (ROC) of 2000 mm, and a concave mirror with a ROC of 1500 mm at one end. The curved mirrors are separated at a distance of 620 mm, resulting in a single-mode diameter of ~2.5 mm (1/e^2) at the Nd:YAG disk. All the flat mirrors are high reflectance at 1.3 μm and high transmittance at 1064 nm so that parasitic lasing and amplified spontaneous emission at 1064 nm are suppressed. Loss control for the two 1.3-μm lines is realized by utilizing a 2720-μm thick quartz as a birefringent filter in the cavity at Brewster's angle. The birefringent filter acts as a high-order waveplate that effectively provides λ/2 retardance for one line and zero or λ retardance for the other line. Consequently, high cavity loss for the 1319-nm line or the 1338-nm line can be controlled by tilting the quartz plate, effectively changing the thickness of the plate. Figure 8 shows the Q-switched output spectra at two different plate angles. To inject/eject the seed to the cavity and prevent self lasing before seed injection, an RTP
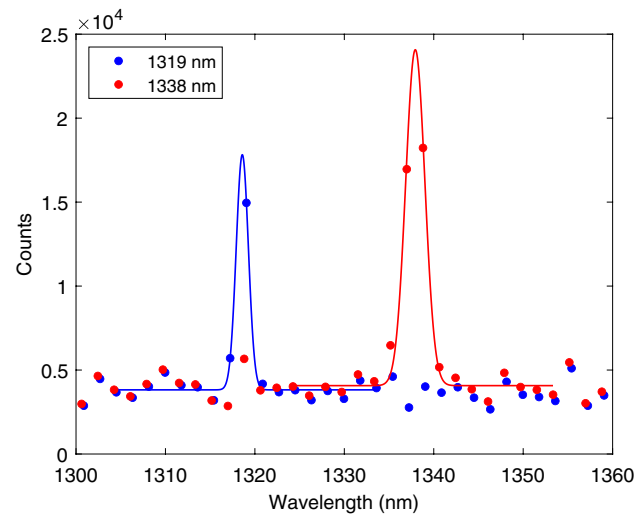

Fig. 8 Measured spectra of 1.3-μm regenerative amplifier operating in *Q*-switched mode. The auxiliary Gaussian lines are fitted and serve as a reference to compensate for the limited resolution of the spectrometer

Fig. 7 Schematic diagram of the 1.3-μm Nd:YAG regenerative amplifier. The optical path of the cavity is denoted in red. *WP* Wollaston polarizer, *PBS* polarizing beamsplitter cube, *BF* birefringent filter, *QWP* quarter-wave plate, *FC* fiber collimator, *FI* Faraday isolator, *DM* dichroic mirror, *DLA* diode laser array
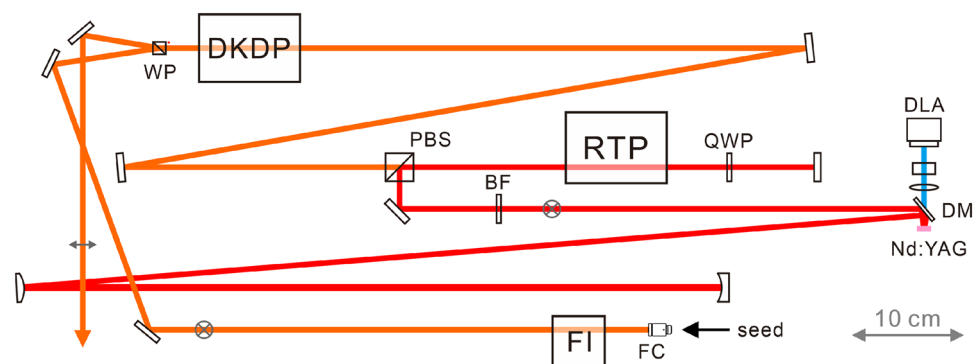
(rubidium titanyl phosphate) Pockels cell driven by a high-voltage square pulse (BEHLKE, Germany), a zero-order quarter-wave plate, and a polarizing beamsplitter cube are placed in the cavity. The cavity round-trip loss is estimated to be ~15% from the transmission data of the intracavity elements. As the input and output ports of the regenerative amplifier for the seed share the same optical path, a DKDP (deuterated potassium dihydrogen phosphate) Pockels cell driven by a 10-ns high-voltage pulse (MOSA Research, Taiwan) and a Wollaston polarizer are implemented to separate the input and output path with an extinction ratio of $>10^3$. Two Faraday isolators with >50 dB isolation are used to reduce feedback to the seed source. The seed is collimated from the optical fiber exit of the intensity modulator to a beam diameter of ~2.5 mm ($1/e^2$) to ensure spatial mode matching with the regenerative amplifier.

Spontaneous emission competes with the seed pulse in a laser amplifier. The spontaneous emission energy in the cavity of the regenerative amplifier can be estimated by calculating the ratio of the divergent solid angle of the cavity mode to the 4π solid angle of spontaneous emissions at 1338 nm [34]. The divergent angle $\theta_d = \lambda/(2\pi r)$ and the divergent solid angle $\Omega_d = \pi\theta_d^2$ of the cavity mode are estimated to be ~1.7×10^{-4} rad and ~9.1×10^{-8} sr, where λ is the wavelength considered, r is the seed beam radius of 1.25 mm. To calculate the emission contribution of the 1338-nm line when pumped at 808 nm, the emission contribution is defined by the product of emission cross section of each line and its linewidth. Then, the emission ratio R_e at 1338 nm, defined by the ratio of the emission contribution at 1338 nm to the total emission contributions of the $^4F_{3/2}$ state, is estimated to be ~3.6% [22]. The radiative quantum efficiency η, defined by the ratio of the fluorescence lifetime to the radiative lifetime of the $^4F_{3/2}$ state, is 0.56 [22]. Only the spontaneous emissions within the cavity round-trip time τ_c of ~14 ns are considered as the regenerative amplifier only opens one round-trip time for seed injection. The spontaneous emission energy E_{sp} at 1338 nm can then be estimated as

$$E_{sp} = N_0 \pi r^2 d\left(1 - \exp\left(-\frac{\tau_c}{T}\right)\right)\frac{\Omega_d}{4\pi}R_e\eta, \tag{2}$$

where d is the thickness of the Nd:YAG crystal and T is the fluorescence lifetime of Nd:YAG. The estimated E_{sp} is ~0.02 fJ which is 4 orders of magnitude lower than the seed energy. Therefore, gain competition from spontaneous emission can be neglected.

The 808-nm diode-pumped Nd:YAG regenerative amplifier boosts the energy of the 0.2-pJ 1338-nm seed to > 6 mJ after ~120 passes of amplification, corresponding to a total gain of 3×10^{10}. A shot-to-shot fluctuation of ~0.7%, measured with a pyroelectric energy meter (J-50MB-LE, Coherent) in 1-minute interval, is achieved. The main source of

the fluctuation may be attributed to thermal disequilibrium and mechanical thermal hysteresis when running the amplifier at a low repetition rate of 2 Hz, set by the repetition rate of our post amplifier chain. Increasing the repetition rate for other applications is possible by improving heat dissipation in the laser system and its driving circuits. The amplified 1338-nm pulse is frequency doubled with ~1% conversion efficiency to measure its temporal profile with a Hamamatsu streak camera. Figure 9 shows that the temporal profile is smooth without multi-longitudinal mode beating. After retrieval, the 1338-nm pulse duration is measured to be ~380 ps. The output beam profile is near TEM_{00} mode, shown in Fig. 10, as expected from a regenerative amplifier with a stable cavity. In accordance with the ISO 11146-1 standard [35], the M^2 parameter is measured with a pyrocamera by focusing the beam with an $f = 100$ cm concave mirror. The results are $M_x^2 \simeq 1.13$ and $M_y^2 \simeq 1.09$ as shown in Fig. 11.

5 Long-wavelength infrared pulse generation

An attractive application of sub-ns 1.3-μm lasers is the generation of LWIR pulses through DFG. As an example, we present calculations for generating energetic 9.2-μm/10.2-μm pulses which is promising for seeding terawatt-class CO_2 amplifiers. The idea of generating energetic LWIR pulses with picosecond duration is to mix sub-ns 1.3-μm single-frequency pulses and sub-ns 1540-nm chirped pulses in a $BaGa_2GeSe_6$ (BGGSe) crystal followed by pulse compression with a grating compressor [8]. BGGSe parameters are listed in Table 1 assuming the pump wavelength of 1318.8 nm/1338.2 nm and the signal wavelength
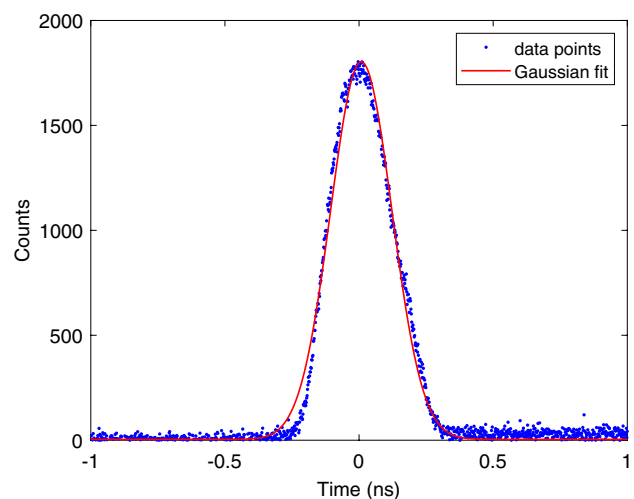

Fig. 9 Measured temporal profile of the frequency-doubled 1338-nm pulse
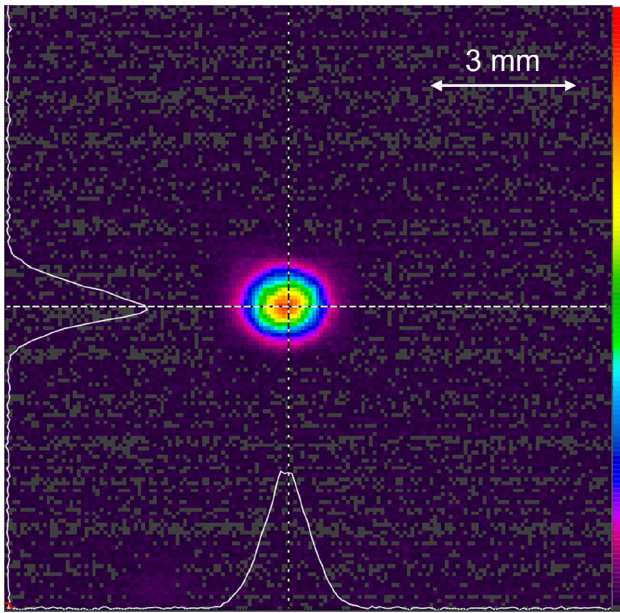
Fig. 10 A typical far-field beam profile of the 1338-nm regenerative amplifier measured with a pyrocamera (PY-III-HR-C-A-PRO, Ophir)
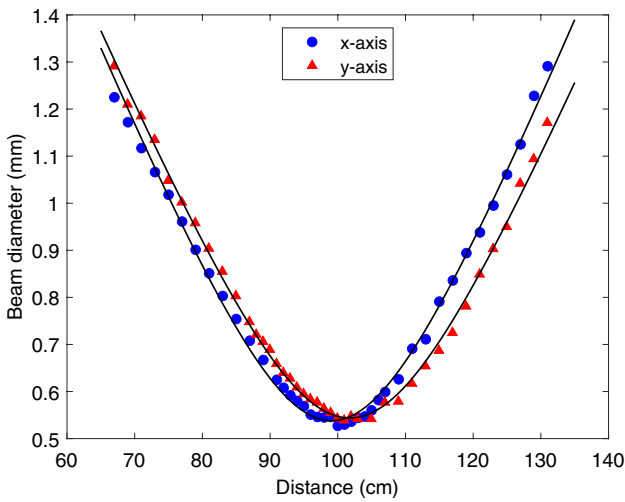

Fig. 11 M^2 measurement showing the laser beam quality at the two axes are $M_x^2 \simeq 1.13$ and $M_y^2 \simeq 1.09$

of 1540 nm. Type-II phase matching is preferable as the effective nonlinear coefficient is larger. To calculate the generated LWIR pulse energy, a code based on the fourth-order Runge–Kutta algorithm with split-step approach [36] is built to solve the coupled-wave equations [37]. As the equations are solved numerically, the code is applicable in the pump depletion regime. Fresnel diffraction [38] calculated by Fourier transformation models the evolution of the beam profile due to spatial walk-off and gain saturation. To ensure consistency, the code is calibrated by comparing with experimental data [8].

In the calculation, we assume that a 1540-nm chirped pulse with 400-μJ energy and 1.6-nm bandwidth is mixed with a 6-mJ 1319-nm/1338-nm single-frequency pulse with a peak intensity of ~1 GW/cm². The beam profiles and temporal profiles are assumed to be Gaussian. The calculated pulse energy of the generated 9.2-μm/10.2-μm chirped pulse is shown in Fig. 12. An idler energy of ~200 μJ with a fluctuation of ~1% can be achieved when the pump and signal fluctuations are 1% and 2%, respectively. Reduction of energy fluctuation is expected in the oversaturated regime [39]. After pulse compression with a grating compressor, a picosecond (<10 ps) 9.2-μm/10.2-μm pulse with an energy exceeding 100 μJ can be obtained.

6 Summary

We present the development of a 400-ps 1338-nm laser comprising a single-frequency intensity-modulated seeding laser and a diode-pumped Nd:YAG regenerative amplifier. Its stable performance has been verified by thorough measurements. The construction of a highly stable pulsed current controller for the high-power pumping laser diode is also reported in detail. The development of 1.3-μm subnanosecond laser with extraordinary energy stability can benefit the field of nonlinear frequency conversion by avoiding two-photon absorption in nonlinear crystals with wide transparency range and reducing intensity fluctuation. An example of generating sub-millijoule picosecond (<10 ps) pulses in the LWIR range is analyzed. By combining this laser and 1540-nm chirped pulses with a polarizing beamsplitter cube and

Table 1 Parameters of BGGSe crystal for 9.2-μm/10.2-μm pulse generation under collinear phase matching. Polarizations are defined as pump − signal = idler. Bandwidth is defined by the phase mismatch $\Delta k = \pm\pi$ at the idler wavelength for a 10-mm-thick crystal. d_{eff} is the maximum effective nonlinear coefficient for this setup

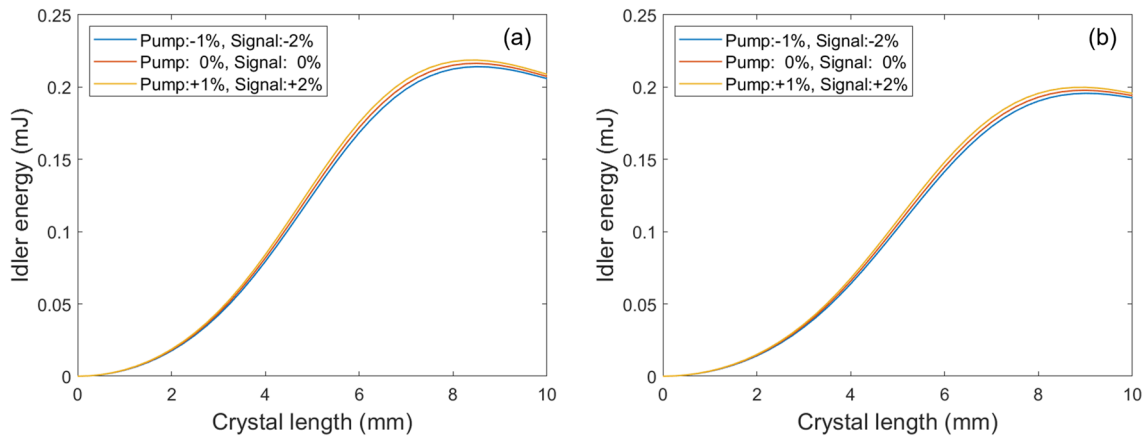| Idler wavelength	Polarizations	Orientations (θ, φ)	Bandwidth	$|d_{\mathrm{eff}}|$
9.2 μm	o − e = e (Type-I)	26.3°, 42.7° †	165 nm	24.1 pm/V
10.2 μm	o − e = e (Type-I)	25.4°, 42.7° †	230 nm	24.5 pm/V
9.2 μm	o − e = o (Type-II)	28.4°, 12.7°	124 nm	35.1 pm/V
10.2 μm	o − e = o (Type-II)	27.3°, 12.7°	170 nm	35.0 pm/V

† φ = −17.3° shows the same $|d_{\mathrm{eff}}|$

Fig. 12 Idler energies of the generated **a** 9.2-μm and **b** 10.2-μm chirped pulses versus crystal length for visualizing fluctuation reduction

then mixing these two lasers in a BGGSe nonlinear crystal under collinear type-II phase matching, more than 100-μJ energy of picosecond 9.2-μm or 10.2-μm pulses after pulse compression in a grating compressor is expected numerically. Such a high-energy LWIR pulse is useful for applications in seeding terawatt-class CO_2 amplifiers.

Code availability Not applicable.

Data availability Data underlying the results presented in this paper are not publicly available at this time but may be obtained from the authors upon reasonable request.

Materials availability Not applicable.

Declarations

Conflict of interest The authors declare no Conflict of interest.

Ethical approval and consent to participate Not applicable.

Consent for publication Not applicable.

References

1. A. Rolle, A. Pereszlenyi, R. Koch, M. Richard, B. Baier, J. Thorac. Cardiovasc. Surg. **131**, 1236–1242 (2006)
2. C. Porrello, R. Gullo, A. Vaglica, G. Scerrino, G. Salamone, L. Licari, C. Raspanti, E. Gulotta, G. Gulotta, G. Cocorullo, Surg. Innov. **25**, 142–148 (2018)
3. J. Boquillon, O. Musset, H. Guillet, S. Roy, *Conference on Lasers and Electro-Optics* (Optica Publishing Group, Washington, 1999), p.CTuK25
4. H. Peng, W. Hou, Y. Chen, D. Cui, Z. Xu, C. Chen, F. Fan, Y. Zhu, Opt. Express **14**, 6543–6549 (2006)
5. S.-B. Dai, M. Chen, S.-J. Zhang, Z.-M. Wang, F.-F. Zhang, F. Yang, Z.-C. Wang, N. Zong, L.-J. Liu, X.-Y. Wang et al., Laser Phys. Lett. **13**, 035401 (2016)
6. C. Kletecka, N. Campbell, C. Jones, J. Nicholson, W. Rudolph, IEEE J. Quantum Electron. **40**, 1471–1477 (2004)
7. A. Zheltikov, J. Phys. B: At. Mol. Opt. Phys. **50**, 092001 (2017)
8. Y.-P. Yang, J.-Y. Lee, J. Wang, Opt. Express **32**, 11182–11192 (2024)
9. Z. Chang, L. Fang, V. Fedorov, C. Geiger, S. Ghimire, C. Heide, N. Ishii, J. Itatani, C. Joshi, Y. Kobayashi et al., Adv. Opt. Photonics **14**, 652–782 (2022)
10. K. Vodopyanov, S. Mirov, V. Voevodin, P. Schunemann, Opt. Commun. **155**, 47–50 (1998)
11. V.V. Badikov, D.V. Badikov, V.B. Laptev, K.V. Mitin, G.S. Shevyrdyaeva, N.I. Shchebetova, V. Petrov, Opt. Mater. Express **6**, 2933–2938 (2016)
12. P. Koch, J. Bartschke, and. J. A. L'huillier: Opt. Express **22**, 13648 (2014)
13. J. Šulc, H. Jelínková, K. Nejezchleb, V. Škoda, Laser Phys. Lett. **2**, 519 (2005)
14. G. Zhang, H. Zhu, C. Huang, J. Chen, Y. Wei, L. Huang, Opt. Lett. **34**, 1495–1497 (2009)
15. Y. Chen, K. Liu, J. Yang, N. Zong, F. Yang, H.-Y. Xu, W. Tu, Z. Liu, Q.-J. Peng, Y. Bo et al., IEEE J. Quantum Electron. **51**, 1–6 (2015)
16. A.M. Rodin, M. Grishin, A. Michailovas, Opt. Laser Technol. **76**, 46–52 (2016)
17. K. Jungwirth, A. Cejnarova, L. Juha, B. Kralikova, J. Krasa, E. Krousky, P. Krupickova, L. Laska, K. Masek, T. Mocek et al., Phys. Plasmas **8**, 2495–2501 (2001)
18. N.N. Yuryshev, Quantum Electron. **26**, 567 (1996)
19. O. Svelto, D.C. Hanna et al., *Principles of Lasers* (Springer, Cham, 2010)
20. M. Zhang, C. Wang, P. Kharel, D. Zhu, M. Lončar, Optica **8**, 652–667 (2021)

21. S.Y. Gus'kov, N.N. Demchenko, A. Kasperczuk, T. Pisarczyk, Z. Kalinowska, T. Chodukowski, O. Renner, M. Smid, E. Krousky, M. Pfeifer et al., Laser Part. Beams **32**, 177–195 (2014)
22. S. Singh, R. Smith, L. Van Uitert, Phys. Rev. B **10**, 2566 (1974)
23. P. Gibbon, E. Förster, Plasma Phys. Control. Fusion **38**, 769 (1996)
24. P. Kaw, Rev. Mod. Plasma Phys. **1**, 1–42 (2017)
25. R. Weigand, H.M. Crespo, Appl. Sci. **5**, 485–515 (2015)
26. W. Lowdermilk, J. Murray, J. Appl. Phys. **51**, 2436–2444 (1980)
27. J.P. Salvestrini, L. Guilbert, M. Fontana, M. Abarkan, S. Gille, J. Light. Technol. **29**, 1522–1534 (2011)
28. P. Horowitz, W. Hill, *The Art of Electronics*, 3rd edn. (Cambridge University Press, Cambridge, 2015)
29. W. Schaper, K. Rudnik, M. Steininger-Fetzer. In 8th European Space Power Conference, vol. 661 of ESA Special Publication H. Lacoste and L. Ouwehand, eds. (2008), p. 17
30. K. Libbrecht, J.L. Hall, Rev. Sci. Instrum. **64**, 2133–2135 (1993)
31. J.H. Dellinger. The temperature coefficient of resistance of copper, 147 (US Government Printing Office) (1911)
32. E. Çadırlı, U. Büyük, H. Kaya, N. Maraşlı, S. Aksöz, Y. Ocak, J. Electron. Mater. **40**, 195–200 (2011)
33. A. Zverev, *Handbook of Filter Synthesis* (Wiley, Amsterdam, 2005)
34. Y.-Y. Hwang, C.-H. Lee, J. Wang, Appl. Opt. **36**, 7802–7808 (1997)
35. ISO 11146-1:2021, Lasers and laser-related equipment – test methods for laser beam widths, divergence angles and beam propagation ratios
36. S. Witte, K.S. Eikema, IEEE J. Sel. Top. Quantum Electron. **18**, 296–307 (2011)
37. J. Armstrong, N. Bloembergen, J. Ducuing, P.S. Pershan, Phys. Rev. **127**, 1918 (1962)
38. M. Born, E. Wolf, *Principles of Optics: Electromagnetic Theory of Propagation, Interference and Diffraction of Light* (Elsevier, Amsterdam, 2013)
39. S. Zhang, M. Fujita, M. Yamanaka, M. Nakatsuka, Y. Izawa, C. Yamanaka, Opt. Commun. **184**, 451–455 (2000)